ACSNANO

www.acsnano.org

ARTICLE

Hierarchically Assembled Cobalt Oxynitride Nanorods and N-Doped Carbon Nanofibers for Efficient Bifunctional Oxygen Electrocatalysis with Exceptional Regenerative Efficiency

Ki Ro Yoon,[¶] Chang-Kyu Hwang,[¶] Seung-hoon Kim,[¶] Ji-Won Jung, Ji Eon Chae, Jun Kim, Kyung Ah Lee, Ahyoun Lim, Su-Ho Cho, Jitendra Pal Singh, Jong Min Kim, Kihyun Shin, Byung Moo Moon, Hyun S. Park, Hyoung-Juhn Kim, Keun Hwa Chae, Hyung Chul Ham, Il-Doo Kim,* and Jin Young Kim*

Cite This: *ACS Nano* 2021, 15, 11218−11230

Read Online

ACCESS | Metrics & More | Article Recommendations | Supporting Information

ABSTRACT: Oxygen-based electrocatalysis is an integral aspect of a clean and sustainable energy conversion/storage system. The development of economic bifunctional electrocatalysts with high activity and durability during reversible reactions remains a great challenge. The tailored porous structure and separately presented active sites for oxygen reduction and oxygen evolution reactions (ORR and OER) without mutual interference are most crucial for achieving desired bifunctional catalysts. Here, we report a hybrid composed of sheath−core cobalt oxynitride (CoO_x@CoN_y) nanorods grown perpendicularly on N-doped carbon nanofiber (NCNF). The brush-like CoO_x@CoN_y nanorods, composed of metallic Co_4N cores and oxidized surfaces, exhibit excellent OER activity (E = 1.69 V at 10 mA cm^{-2}) in an alkaline medium. Although pristine NCNF or CoO_x@CoN_y alone had poor catalytic activity in the ORR, the hybrid showed dramatically enhanced ORR performance (E = 0.78 V at −3 mA cm^{-2}). The experimental results coupled with a density functional theory (DFT) simulation confirmed that the broad surface area of the CoO_x@CoN_y nanorods with an oxidized skin layer boosts the catalytic OER, while the facile adsorption of ORR intermediates and a rapid interfacial charge transfer occur at the interface between the CoO_x@CoN_y nanorods and the electrically conductive NCNF. Furthermore, it was found that the independent catalytic active sites in the CoO_x@CoN_y/NCNF catalyst are continuously regenerated and sustained without mutual interference during the round-trip ORR/OER, affording stable operation of Zn−air batteries.

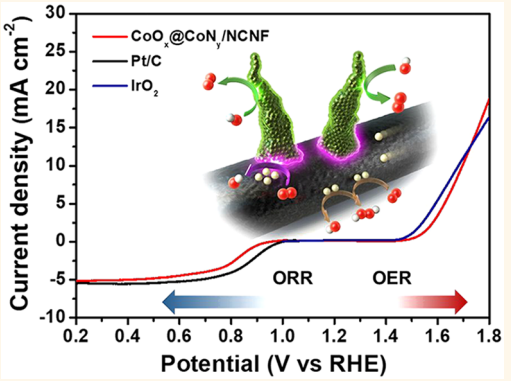

KEYWORDS: *cobalt oxynitrides, carbon nanofibers, bifunctional catalysts, oxygen reduction reaction, oxygen evolution reaction*

INTRODUCTION

Oxygen-based electrocatalysis, which drives oxygen reduction and oxygen evolution reactions (ORR and OER), is an integral process in many key clean and renewable energy technologies, including fuel cells, water electrolyzers, and metal−air batteries.[1−4] ORR is a half-reaction at the cathode in fuel cells, and it is also the major limiting factor with regard to fuel-cell performance. OER is an anodic half-reaction in water electrolyzers, and it occurs in conjunction with the hydrogen evolution reaction (HER). Metal−air batteries have greater technological challenges because they require a recharging operation; in these batteries, ORR occurs during the discharge step, with the reverse process (OER) taking place at the same electrode when the battery is charging.

Received: November 25, 2020
Accepted: June 14, 2021
Published: June 18, 2021

https://doi.org/10.1021/acsnano.0c09905
ACS Nano 2021, 15, 11218−11230

Traditionally, noble metals (such as Pt and Pt-alloys) and metal oxides (such as IrO_2 and RuO_2) have been employed to increase the reaction kinetics and improve the ORR and OER performance outcomes, respectively. Unfortunately, most noble-metal-based catalysts only exhibit catalytic activity for a single reaction,[5] which limits their use as catalysts in metal−air batteries, and two species are physically mixed to facilitate both the ORR (in the discharge state) and the OER (in the recharge state). Additionally, the materials' high cost, earth-scarcity, and poor durability during the reactions make them impracticable for widespread commercialization. This has led to an increased level of demand for nonprecious and multifunctional electrocatalysts in a single catalytic unit.[6−8]

Heteroatom-doped carbons such as nitrogen (N) dopants and/or transition metals (TMs = Co, Fe, and Mn, *etc.*) incorporated into graphene planes to form N−C or TM−N−C catalysts have been artificially devised to reduce the cost and enhance the catalytic activities during the ORR and/or OER.[9−14] Considerable efforts have been devoted to improving ORR/OER performance outcomes, and the chemical interactions between the dopant species and the surrounding carbon complex are the principal factors to consider when modulating the binding energies of the reaction intermediates (*OH, *O, and *OOH)[15−17] and attempting to realize outstanding catalytic activity.[18] Unfortunately, a precisely designed active site in a single catalytic unit is essentially active toward a *one-way* reaction. This requires two or more functional sites in the local atomic structure, but accomplishing that remains a great technological challenge.[19] Importantly, the durability of the catalysts in metal−air batteries also remains a critical issue, as a single catalytic active site is highly susceptible to electrochemical transformation during the dynamic reverse reaction. As far as we are aware, at present, in-depth research has rarely focused on the sustainability of active sites along with the regeneration with prolonged cycles.

Recently, hybrids composed of carbonaceous materials with TM-based binary or ternary alloys,[20] and their oxides,[21−23] have been developed as cost-effective bifunctional catalysts. Following the pioneering work of Dai *et al.*, various N-doped carbon-supported Co_3O_4 bifunctional electrocatalysts have been reported.[24] Unlike physical mixtures of Co_3O_4 and N-doped reduced graphene oxide (rGO), which exhibit little ORR activity, unexpectedly high activities toward both the ORR and OER were obtained through a hybridization strategy. Although the ORR mechanism remains unclear, the results provided an indispensable clue that the synergistic coupling between active Co_3O_4 and an N-doped carbon material is responsible for the exceptional ORR activity. Nevertheless, little progress has been made toward enhancing the ORR activity to levels comparable to those of precious-metal-based catalysts due to the reduced accessibility of unexposed catalytic active sites when these materials are hybridized and the inherently low electrical conductivity of supported inorganic oxide particles. Furthermore, it is likely that the original structure would collapse and the activities would degrade during the operation of a reversible metal−air battery. Several requirements should be met simultaneously to achieve bifunctional ORR/OER activities and durability, including the formation of individual active sites for the ORR and OER with high accessibility to the reaction intermediates, sufficient stability of those structures under reversible reactions, and definite electrical connections between hybridized components.

Herein, we present a hybrid consisting of hierarchically assembled brush-like sheath (CoO_x)−core(CoN_y) cobalt oxynitride (CoO_x@CoN_y) nanorods immobilized directly on electrospun N-doped carbon nanofiber (NCNF) as a high-performance and durable bifunctional electrocatalyst in alkaline media. The proposed CoO_x@CoN_y/NCNF hybrid exhibited outstanding ORR/OER activity in half-cell measurements and in various full-cell applications (alkaline membrane fuel cells, water electrolyzers, and Zn−air batteries). We provide direct experimental and theoretical evidence of synergistic coupling effects on the bifunctionality and regenerative efficiency of active sites. For example, CoO_x@CoN_y nanorods exhibited high activity toward OER, which was attributed to the facile charge transfer at the metallic Co_4N core part and the numerous OER active sites on the oxidized nanorod surfaces.[25] Significantly, the freestanding growth of CoO_x@CoN_y nanorods on NCNF provides favorable interfacial adsorption sites for ORR intermediates as well as highly electrical charge transport channels. Finally, we demonstrate that high durability of CoO_x@CoN_y/NCNF was achieved with the aid of independently existing and regenerative active sites for the ORR and OER, without mutual interference, in the hybrid electrocatalyst.

RESULTS/DISCUSSION

Figure 1a illustrates the fabrication processes of CoO_x@CoN_y/NCNFs obtained at different nitridation temperatures. First, one-dimensional (1D) N-doped CNF (NCNF) paper was synthesized by electrospinning polyacrylonitrile (PAN) dissolved in a dimethylformamide (DMF) solution with a subsequent carbonization process.[25] The obtained NCNF paper was immersed in a dopamine solution at room temperature to form a uniform polydopamine (PD) coating layer on the surface. The solution color turned from pale brown to dark brown after 12 h of the polymerization of dopamine (Supporting Information Figure S1a). The increases in the O 1s and N 1s peaks in the X-ray photoelectron spectroscopy (XPS) survey scan are attributed to the catechol and amide functional groups of PD, respectively, on NCNF (Figure S1b). The surface of the PD-treated NCNF has more hydrophilic features than the initial pristine NCNF,[26] facilitating hydrothermal growth on this surface. Next, the PD-treated NCNF was placed into a 50 mL autoclave, and certain amounts of cobalt(II) nitrate, urea, and NH_4F were added to the solution. The sealed autoclave was heated to 120 °C for 6 h, after which rod-like Co(OH)Fs formed perpendicularly on the NCNF. Finally, the obtained Co(OH)F/NCNF was thermally annealed at various nitridation temperatures (450, 550, and 650 °C) in an Ar-filled tube furnace with an ammonia (NH_3) gas flow. The series of CoO_x@CoN_y/NCNFs was designated as CoO_x@CoN_y/NCNF450, CoO_x@CoN_y/NCNF550, and CoO_x@CoN_y/NCNF650, depending on the nitridation temperature. The percentage by weight of CoO_x@CoN_y nanorods grown on the NCNF was approximately 79.5 wt %, as confirmed by a thermogravimetric analysis (TGA) (Figure S2).

The microstructural features of the NCNF, Co(OH)F/NCNF, and CoO_x@CoN_y/NCNF series were characterized by means of scanning electron microscopy (SEM) and transmission electron microscopy (TEM) analyses. The electrospun NCNF exhibits a consistently elongated 1D fibrous shape with a smooth surface and an average diameter of approximately 500 nm (Figure 1b). After the hydrothermal reaction, perpendicularly grown and densely assembled bundles of Co(OH)F nanorods were observed along the trace of the NCNF (Figure

https://doi.org/10.1021/acsnano.0c09905
ACS Nano 2021, 15, 11218−11230

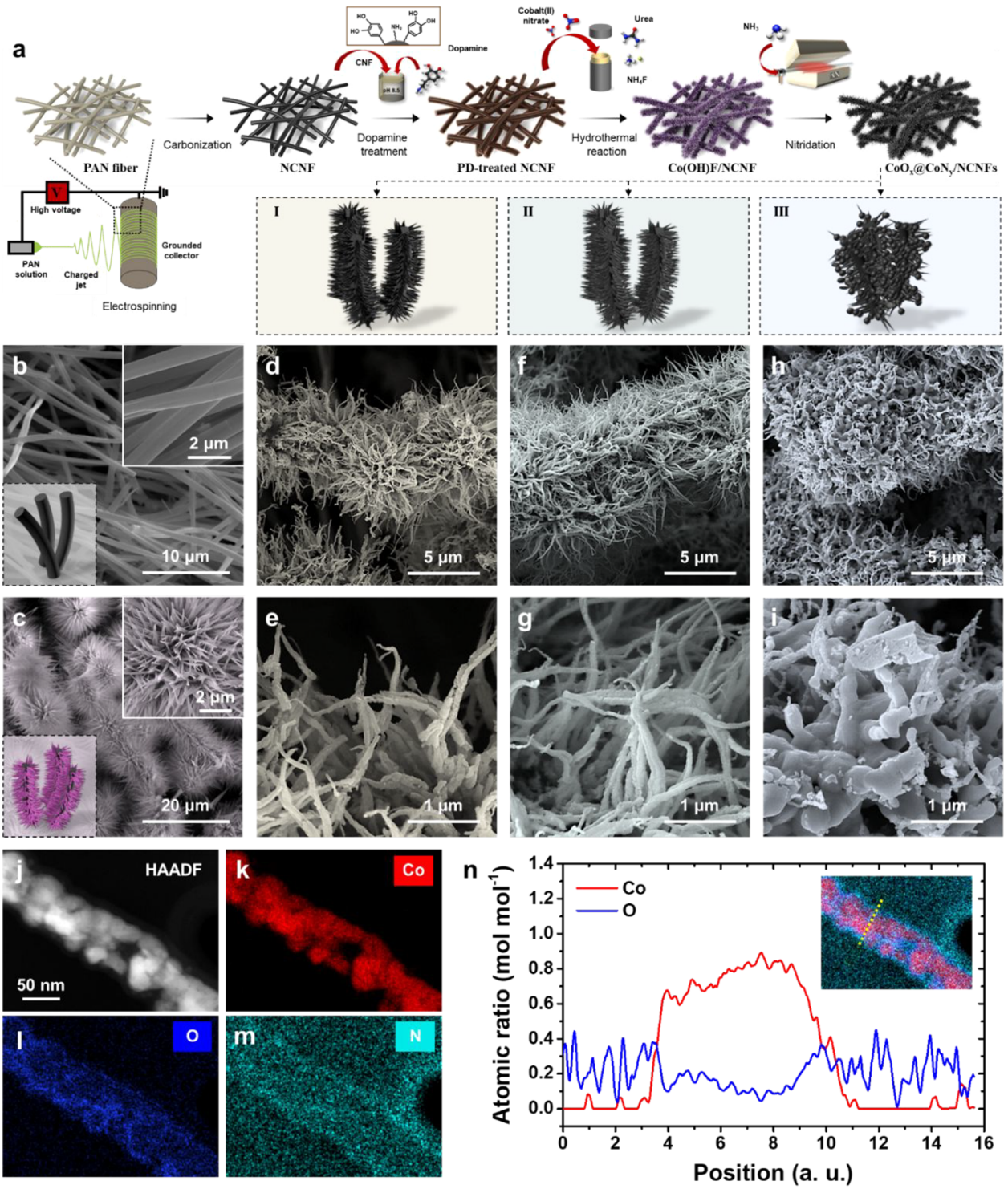

Figure 1. (a) Schematic illustration of the fabrication processes of $CoO_x@CoN_y$/NCNFs (I, $CoO_x@CoN_y$/NCNF450; II, $CoO_x@CoN_y$/NCNF550; III, $CoO_x@CoN_y$/NCNF650). SEM images of (b) NCNF, (c) Co(OH)F/NCNF, (d, e) $CoO_x@CoN_y$/NCNF450, (f, g) $CoO_x@CoN_y$/NCNF550, and (h, i) $CoO_x@CoN_y$/NCNF650. (j) HAADF-STEM, and EDS elemental mapping images of (k) Co, (l) O, and (m) N atoms. (n) Line scan profile images of $CoO_x@CoN_y$ nanorods in $CoO_x@CoN_y$/NCNF550.

1c). As the final products, the phase-transformed $CoO_x@CoN_y$/NCNFs following the nitridation process exhibited crumpled and crystallized nanorods. We found that brush-like $CoO_x@CoN_y$ nanorods with an average diameter close to 50 nm and a length in the range of 2−5 μm were similarly obtained from the 450 and 550 °C nitridation process (Figures 1d−g). These brush-like nanorods are self-supported on the NCNF without any polymeric binders and can therefore provide close electrical contact and numerous accessible sites for reaction intermediates during the electrocatalysis process. Compared to $CoO_x@CoN_y$/NCNF450 and $CoO_x@CoN_y$/NCNF550, severe grain growth of nanorods was observed on $CoO_x@CoN_y$/NCNF650 (Figure 1h,i), which may reduce the accessible surface area and pores between the brushes and the NCNFs.

https://doi.org/10.1021/acsnano.0c09905
ACS Nano 2021, 15, 11218−11230

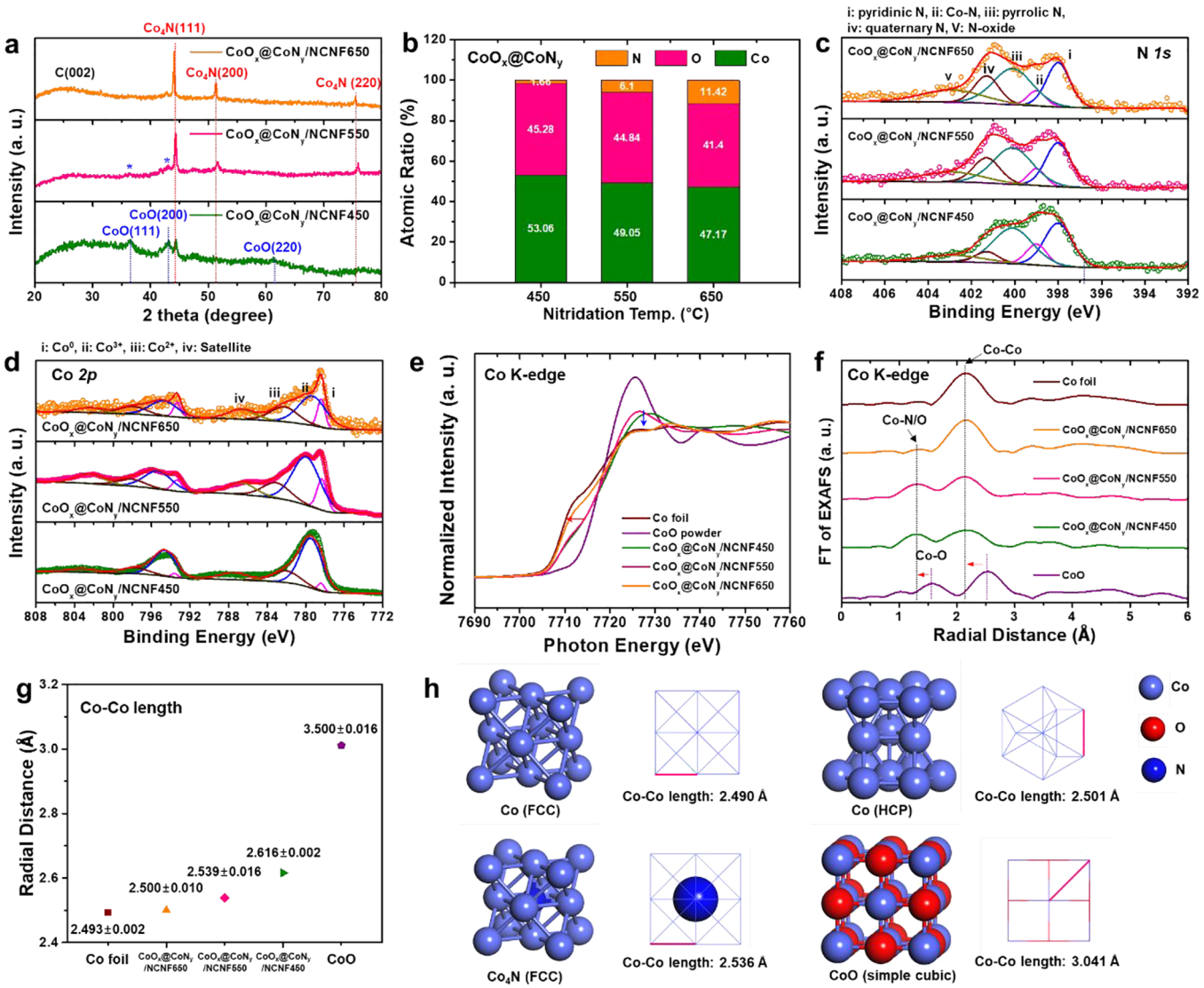

Figure 2. (a) XRD patterns of CoO_x@CoN_y/NCNF series. (b) Relative atomic ratios between N, O, and Co in CoO_x@CoN_y series. XPS spectra in (c) N 1s and (d) Co 2p region for CoO_x@CoN_y/NCNF series. (e) Co *K*-edge XANES spectra, (f) simulated EXAFS-FT spectra, and (g) calculated Co−Co bond length for CoO_x@CoN_y/NCNF series with Co foil and CoO powder as references. (h) Crystal structures of Co (FCC), Co (HCP), Co_4N (FCC), and CoO (simple cubic) with a simulated Co−Co bond length.

The atomic distribution of the synthesized materials was analyzed by energy dispersive X-ray spectrometry (EDS) mapping. The CoO_x@CoN_y nanorod in the high-angle annular dark-field scanning transmission electron microscopy (HAADF-STEM) image in Figure 1j shows the internal homogeneous distribution of Co, O, and N (Figure 1k−m). The EDS line scanning profile along the line drawn across the nanorod shows that a high density of O atoms existed at the surficial region of the nanorods (Figure 1n), indicating that an oxide layer had formed on the surface of the CoO_x@CoN_y nanorods after the nitridation process. It was also noted that the thickness of the oxide layer decreased with an increase in the nitridation temperature (Figure S3).

As shown in the TEM images, the nanorods in the CoO_x@CoN_y/NCNF series consist of small interconnected polycrystalline grains (Figure S4). The main body of the nanorods shows a lattice spacing between 2.051 and 2.062 Å in the high-resolution TEM (HRTEM) images, which corresponds to the (111) plane of a previously reported cobalt nitride (Co_4N).[27,28] Interestingly, lattice spacings of 2.133 and 2.430 Å were detected at the outer part of the nanorods in the CoO_x@CoN_y/NCNF450 and CoO_x@CoN_y/NCNF550 samples (Figure S4c,f), which correspond to the (200) and (111) facets of CoO, respectively.[25] This observation is in good agreement with the aforementioned EDS mapping results of the CoO_x@CoN_y nanorods.

Furthermore, ring patterns in the selected-area electron diffraction (SAED) result of CoO_x@CoN_y/NCNF550 (Figure S5) also suggest that the nanorods consisted of composite crystallites of Co_4N, as indicated by the (111), (200), and (220) planes, and a certain portion of the CoO phase on the surface, as evidenced by the blurred dots for (111) and (220). These observations overall reveal that the nanorods have a sheath (CoO_x)−core (Co_4N) structure after nitridation, but there were fewer surficial oxide species and the grain size increased with an increase in the nitridation temperature. As a control sample, we also prepared fully oxidized CoOx/NCNF550 *via* the thermal oxidation of Co(OH)F/NCNF at 550 °C in air. As shown in Figure S6, the overall nanorod morphology was well-maintained, an outcome similar to that with CoO_x@CoN_y/NCNFs, but the lattice fringe and SAED patterns indicated that

https://doi.org/10.1021/acsnano.0c09905
ACS Nano 2021, 15, 11218−11230

polycrystalline nanorods are composed of both CoO and Co_3O_4 phases in CoOx/NCNF550.

The crystalline phases of CoO_x@CoN_y/NCNF450, CoO_x@CoN_y/NCNF550, and CoO_x@CoN_y/NCNF650 were analyzed according to the X-ray diffraction (XRD) patterns (Figure 2a). The broad shoulder that appeared at 20−30° in all samples was attributed to the (002) planes of turbostratic carbon in NCNF.[25] For CoO_x@CoN_y/NCNF450, relatively weak crystalline peaks were observed at 36.5, 42.4, and 61.5° and were assigned to the (111), (200), and (220) planes of CoO (JCPDF No. 43-1004), respectively. With an increase in the nitridation temperature, three peaks at around 44.2, 51.5, and 75.8° became dominant, corresponding to the (111), (200), and (220) planes of face-centered cubic (FCC) structured metallic Co (JCPDF No. 15-0806) or cobalt nitrides, as presented in Figure 2g.[29−31] Metallic Co naturally has a hexagonal close-packed (HCP) and FCC structure, as depicted in Figure 2h. It has been reported that the N atoms can be incorporated into metallic Co by the experimental (RF-sputtering or thermal nitridation process)[32,33] or computational methods,[34] forming various cobalt nitride phases (*e.g.*, CoN, Co_2N, Co_3N, and Co_4N). When N is doped into the Co at approximately a 4:1 atomic ratio, *i.e.*, Co_4N, the FCC structure is maintained, with N atoms positioned at the center of six Co atoms, causing the expansion of the lattice distance, as depicted in Figure 2h.[25,35] The degree of N doping into the Co lattice can also be deduced by the shift of the peaks in the XRD pattern. An increase in the nitridation temperature leads to a negative shift of the diffraction peaks, implying the lattice expansion of metallic Co caused by addition of N atoms. This result is in good agreement with our TEM observation (Figure S4). The peak positions of CoO_x@CoN_y/NCNF650 at 44.00, 51.22, and 75.36°, respectively, are similar to those of the (111), (200), and (220) planes for Co_4N in earlier studies.[28,29,36]

The precise dopant ratio and chemical composition of the cobalt-based nanorods were deduced from the XPS analysis of the CoO_x@CoN_y series without NCNF, which was excluded because the PAN-driven NCNF inherently includes N and O atoms in its turbostratic carbon structure (Figure S1). The samples in the CoO_x@CoN_y series were synthesized *via* a hydrothermal reaction without a NCNF substrate followed by the same nitridation step (Figure S7). The obtained CoO_x@CoN_y series exhibited a similar rod-like structure but also showed a nondirectional morphology (Figure S8). As shown in Figure 2b, the amount of nitrogen increased with an increase in the nitridation temperature and reached 11.42 at. % upon nitridation at 650 °C. On the basis of the XPS results, we presumed that the *x* and *y* values in CoO_x@CoN_y/NCNF450, CoO_x@CoN_y/NCNF550, and CoO_x@CoN_y/NCNF650 would be $CoO_{0.85}N_{0.03}$/NCNF, $CoO_{0.91}N_{0.12}$/NCNF, and $CoO_{0.87}N_{0.24}$/NCNF, respectively.

To elucidate the surface chemical bonding structures, we conducted a further XPS analysis of the CoO_x@CoN_y/NCNF series, specifically focusing on the N 1s, Co 2p, and C 1s regions; the quantitative data are summarized in Table S1. For the N 1s spectra, various N functionalities, *i.e.*, pyridinic N (~398.15 eV), pyrrolic (~400.86 eV), graphitic (~401.51 eV), and oxidized N (~403.73 eV), were observed, which are ascribed to the PAN-driven NCNF backbone (Figure S9), while the Co−N_x (~399.16 eV) peak is related to the CoO_x@CoN_y nanorods.[25] It has been reported that quaternary N and the surrounding carbon moiety show catalytic activity toward both the ORR or OER,[37] whereas pyrrolic and pyridinic sites are dominated by naturally doped N from the decomposed PAN precursor in the turbostratic carbon structure in pristine NCNF. With an increase in the synthetic temperature, the deconvoluted areal ratio of graphitic N increased. This was deduced from the graphitization of turbostratic carbon in the NCNF backbone. Similarly, the C 1s region became dominated by C−C/C═C bonds (~284.68 eV) as the temperature was increased (Figure S10). As shown in Figure 2d, the Co 2p was deconvoluted into the Co^0, Co^{3+}, and Co^{2+} and satellite peaks as indicated by i, ii, iii, and iv, respectively, and all peaks appeared as doublets. Here, Co^{2+} corresponds to CoO at the surface of the CoO_x@CoN_y nanorods, but the existence of Co^{3+} indicates that further oxidized or amorphous cobalt oxide phases are also present. It should be noted that the proportion of metallic Co^0 increased gradually from 3.06 to 14.54 at. %, whereas the sum of Co^{2+} and Co^{3+} decreased from 80.84 to 66.60 at. % (from CoO_x@CoN_y/NCNF450 to CoO_x@CoN_y/NCNF650), implying a phase transition from CoO_x to metallic Co (actually Co_4N), also in good agreement with the XRD results.

X-ray absorption spectroscopy (XAS) was employed to investigate the local structure of the samples. Figure 2e presents the X-ray absorption near-edge structure (XANES) at the Co *K*-edge of CoO_x@CoN_y/NCNF450, CoO_x@CoN_y/NCNF550, and CoO_x@CoN_y/NCNF650 with Co foil and CoO powder as references. With an increase in the nitridation temperature, a negative pre-edge shift was observed in the XANES spectra (as marked by the red arrow). The CoO_x@CoN_y/NCNF650 spectrum showed edge features that were similar to those of the metallic Co foil, which underscores the metallic nature of Co_4N.[38] Additionally, the decrease in the white-line area (as indicated by the blue arrow) is also attributed to the well-ordered FCC coordination of Co−Co bonds with fewer 3d hole vacancies.[39]

Further differences in the local structure of the catalysts can be seen in the extended X-ray absorption fine-structure (EXAFS) spectra (Figure 2f) and the corresponding K^2-weighted EXAFS spectra (Figure S11). Co−Co bonding at 2.14 Å was evident in CoO_x@CoN_y/NCNF450, CoO_x@CoN_y/NCNF550, and CoO_x@CoN_y/NCNF650, with some differences in the peak intensities. The peak from Co−N bonding was not clearly distinguished from that of Co−O bonding, but the negative shift from Co−O bonding at 1.64 Å is presumably due to the interaction with Co−N/O bonding. The decrease in the Co−N/O peak intensity may be evidence of the escape of O and N atoms in CoO_x@CoN_y/NCNF650, which is clearly supported by the derived Co−Co radial length, as displayed in Figure 2g. CoO has a Co−Co bond length of approximately 3.50 Å. As the nitridation temperature was increased, the bond length of Co−Co was reduced (to ~2.62, ~2.54, and ~2.50 Å for CoO_x@CoN_y/NCNF450, CoO_x@CoN_y/NCNF550, and CoO_x@CoN_y/NCNF650, respectively). This finding implies the desorption of N and O atoms and the formation of a metallic Co phase, approaching the value of Co foil with a Co−Co bond length of 2.49 Å. Compared to the simulated Co−Co length (2.54 Å) in the Co_4N crystalline structure (Figure 2i), the closest Co−Co length value occurred in CoO_x@CoN_y/NCNF550.

To evaluate the bifunctional electrocatalytic activities of the prepared samples, we took half-cell measurements using a three-electrode system. Catalysts loaded on a glassy carbon electrode (GCE), Pt wire, and a standard calomel electrode (SCE) were utilized as the working, counter, and reference electrodes, respectively. These electrodes were immersed in a 0.1 M KOH solution as an electrolyte, which was purged by O_2 gas for the

https://doi.org/10.1021/acsnano.0c09905
ACS Nano 2021, 15, 11218−11230

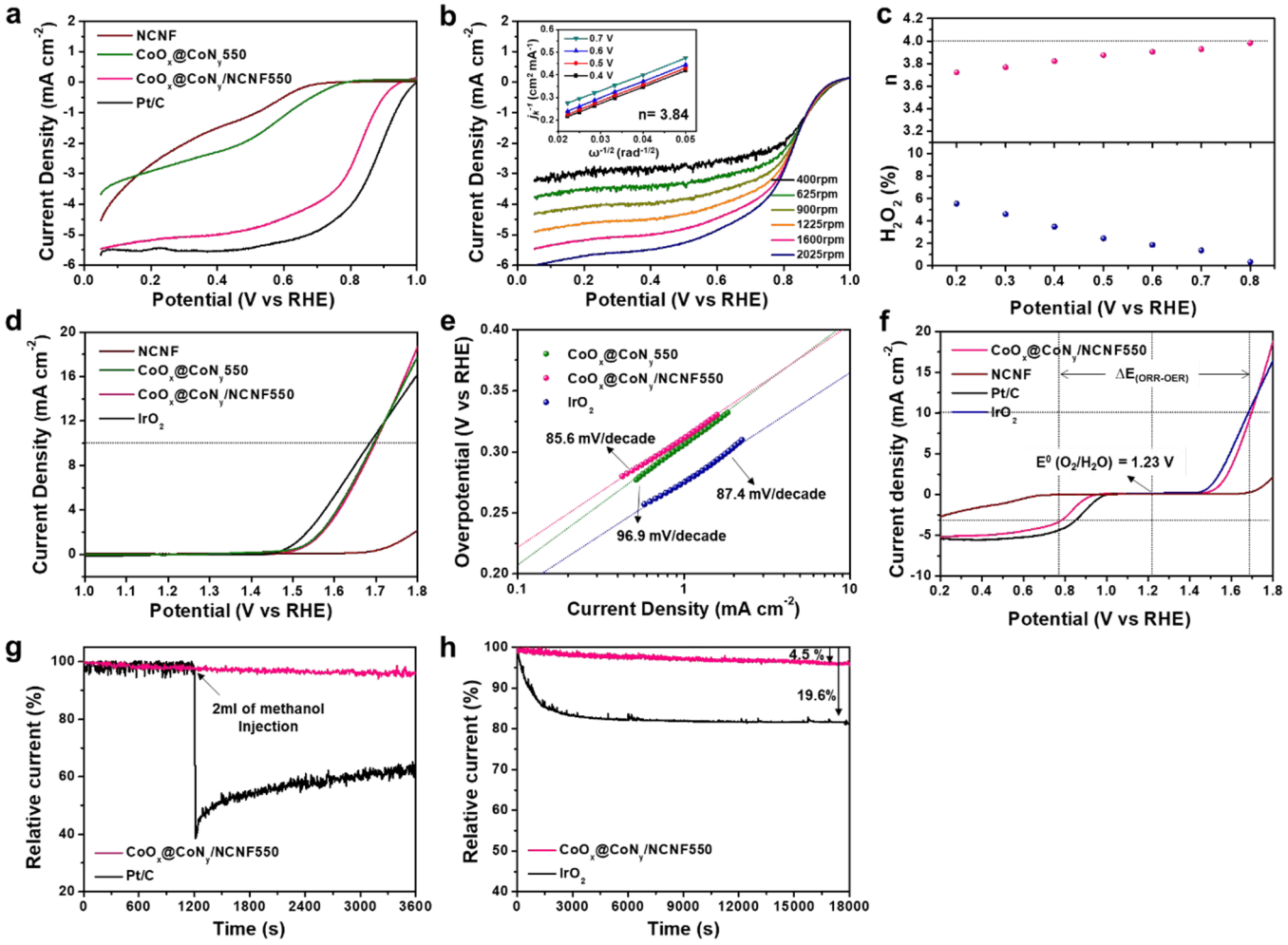

Figure 3. Electrochemical ORR and OER performance and stability results in 0.1 M KOH. (a) ORR polarization curves for NCNF, CoO_x@CoN_y550, CoO_x@CoN_y/NCNF550, and Pt/C. (b) ORR curves at different rotation speeds (inset, K−L plots). (c) RRDE test for CoO_x@CoN_y/NCNF550. (d) OER polarization curves for NCNF, CoO_x@CoN_y550, CoO_x@CoN_y/NCNF550, and IrO_2. (e) Tafel plots of CoO_x@CoN_y550, CoO_x@CoN_y/NCNF550, and IrO_2 and (f) LSVs of CoO_x@CoN_y/NCNF550, IrO_2, and Pt/C revealing bifunctional electrocatalytic activity toward ORR/OER. Chronoamperometric responses of (g) CoO_x@CoN_y/NCNF550 and commercial Pt/C at 0.63 V of ORR overpotential upon the introduction of 2 mL of methanol and (h) CoO_x@CoN_y/NCNF550 and commercial IrO_2 at 0.37 V of OER overpotential in O_2 saturated 0.1 M KOH at a rotation rate of 1600 rpm.

ORR or Ar gas for the OER. First, we compared the ORR and OER performance outcomes between the prepared CoO_x@CoN_y/NCNF series (CoO_x@CoN_y/NCNF450, CoO_x@CoN_y/NCNF550, and CoO_x@CoN_y/NCNF650) and fully oxidized CoO_x/NCNF550. As shown in Figure S12, CoO_x@CoN_y/NCNF550 exhibited the best activities for both the ORR and OER among the CoO_x@CoN_y/NCNFs series, while CoO_x/CNF550 showed the worst performance in both the ORR and OER. These preliminary results indicated that the nitridation step is essential for enhancing the catalytic function by forming the CoO_x@CoN_y hybrid structure in nanorods. Detailed discussions related to this are included in Figure S12.

To decouple the activities of the CoO_x@CoN_y nanorods and NCNF, the ORR and OER performances of pristine CoO_x@CoN_y nanorods (CoO_x@CoN_y550) and NCNF were further evaluated and compared with that from commercial Pt/C (20%) or IrO_2. The CoO_x@CoN_y550 was prepared, followed by a similar hydrothermal method and subsequent nitridation process with CoO_x@CoN_y/NCNF550 without the addition of NCNF. Figure 3a presents linear scan voltammograms (LSVs) of NCNF, CoO_x@CoN_y550, CoO_x@CoN_y/NCNF550, and Pt/C for the ORR, where the corresponding onset potentials were 0.76, 0.80, 0.95, and 1.00 V *versus* a reversible hydrogen electrode (V_{RHE}). Pristine electrospun NCNF showed poor ORR activity, as reported in previous studies.[17,40] Notably, CoO_x@CoN_y550 exhibited much lower electrocatalytic activities than CoO_x@CoN_y/NCNF550. These results strongly suggest that CoO_x@CoN_y and NCNF have a synergistic influence on the ORR.

The LSV curves at various rotation speeds clearly indicate the activity of CoO_x@CoN_y/NCNF550, exhibiting a linear increase in the ORR activity with an increase in the rotation speed. The electron-transfer number (n) for the ORR was calculated from Koutecky−Levich (K−L) plots. As shown in the inset of Figure 3b, there was a linear relationship between J_k^{-1} and $\omega^{-1/2}$, where J_k and ω correspond to the kinetic current density and the electrode angular speed, respectively. The calculated n value for CoO_x@CoN_y/NCNF550 was 3.84, which was somewhat comparable to that of state-of-the-art Pt/C catalyst (n = 4.0) (Figure S13). The n value of CoO_x@CoN_y/NCNF550 was also confirmed by means of rotating ring disk electrode (RRDE) tests. Figure S14 presents the measured disk and ring current

https://doi.org/10.1021/acsnano.0c09905
ACS Nano 2021, 15, 11218−11230

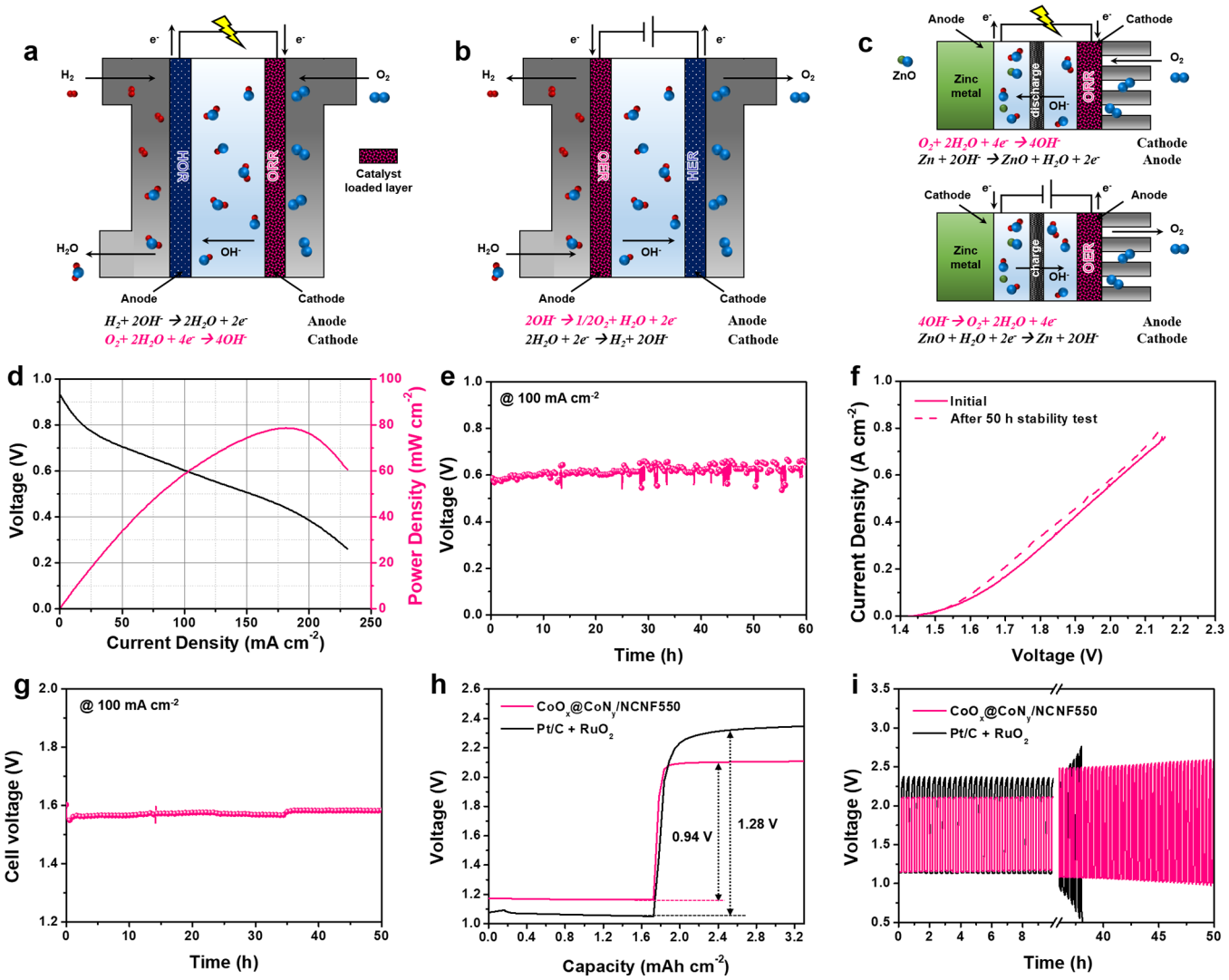

Figure 4. Schematic configurations of full-cell devices for oxygen electrocatalysis and their reaction mechanisms: (a) alkaline membrane fuel cell (AMFC), (b) water electrolyzer (WE), and (c) Zn−air battery (ZAB) with catalyst loaded electrodes. (d) Polarization curves and (e) chronopotentiometry performance of CoO_x@CoN_y/NCNF550-coated MEA in AMFC. (f) Polarization curves before and after 50 h stability test and (g) chronopotentiometry performance of CoO_x@CoN_y/NCNF550 in WE. (h) Initial discharge and charge curves and (i) discharge/charge cyclic performances of CoO_x@CoN_y/NCNF550 and "Pt/C + IrO_2" cathodes in ZAB.

densities of CoO_x@CoN_y/NCNF550, and Figure 3c presents the calculated *n* values and the amounts of H_2O_2 that evolved (%) at the selective potentials.[41] The evolved H_2O_2 gas generated *via* the $2e^-$ transfer during the ORR remained at less than 6%, and the determined average *n* value was 3.89, demonstrating high efficiency and selectivity for the ORR of the CoO_x@CoN_y/NCNF550 catalyst.

Figure 3d presents the LSVs of NCNF, CoO_x@CoN_y550, CoO_x@CoN_y/NCNF550, and the commercial IrO_2 catalyst in the OER potential region. The NCNF has mostly negligible OER activity, while exceptional OER performance was obtained from the CoO_x@CoN_y-containing catalyst samples. The potentials measured at an anodic current density of 10 mA cm^{-2} for CoO_x@CoN_y550, and CoO_x@CoN_y/NCNF550 is 1.69 V, and that for pristine NCNF exceeded 1.80 V. These results suggest that the CoO_x@CoN_y components mainly contribute to the OER, showing performance comparable to that of the IrO_2 catalyst (E = 1.68 V at 10 mA cm^{-2}). The excellent reaction kinetics of CoO_x@CoN_y/NCNF550 is reflected in the Tafel plot (Figure 3e). CoO_x@CoN_y/NCNF550 shows a Tafel slope of ~85.6 mV $decade^{-1}$, which is lower than those of IrO_2 (87.4 mV $decade^{-1}$) and CoO_x@CoN_y550 (96.9 mV $decade^{-1}$). This indicates that CoO_x@CoN_y/NCNF550 facilitates rapid OER kinetics by reducing the activation barrier to the rate-determining step (RDS), while NCNF offers a facile and efficient reaction pathway during the OER.

Bifunctional electrocatalytic behavior is generally evaluated using the potential gap between the ORR current density of −3 mA cm^{-2} and the OER current density of 10 mA cm^{-2}, as represented by $\Delta E_{(ORR-OER)}$ in Figure 3f.[6] A small ΔE value indicates a well-balanced high-performance bifunctional electrocatalyst, potentially beneficial for practical applications. The ΔE value of CoO_x@CoN_y/NCNF550 was determined to be 0.91 V, which is comparable to the gap between the ORR current density of Pt/C and the OER current density of IrO_2 (0.85 V). Both are known to be state-of-the-art ORR and OER active catalysts. Moreover, such a small ΔE is also comparable to those of recently reported outstanding Co-based bifunctional electrocatalysts (Table S2).

https://doi.org/10.1021/acsnano.0c09905
ACS Nano 2021, 15, 11218−11230

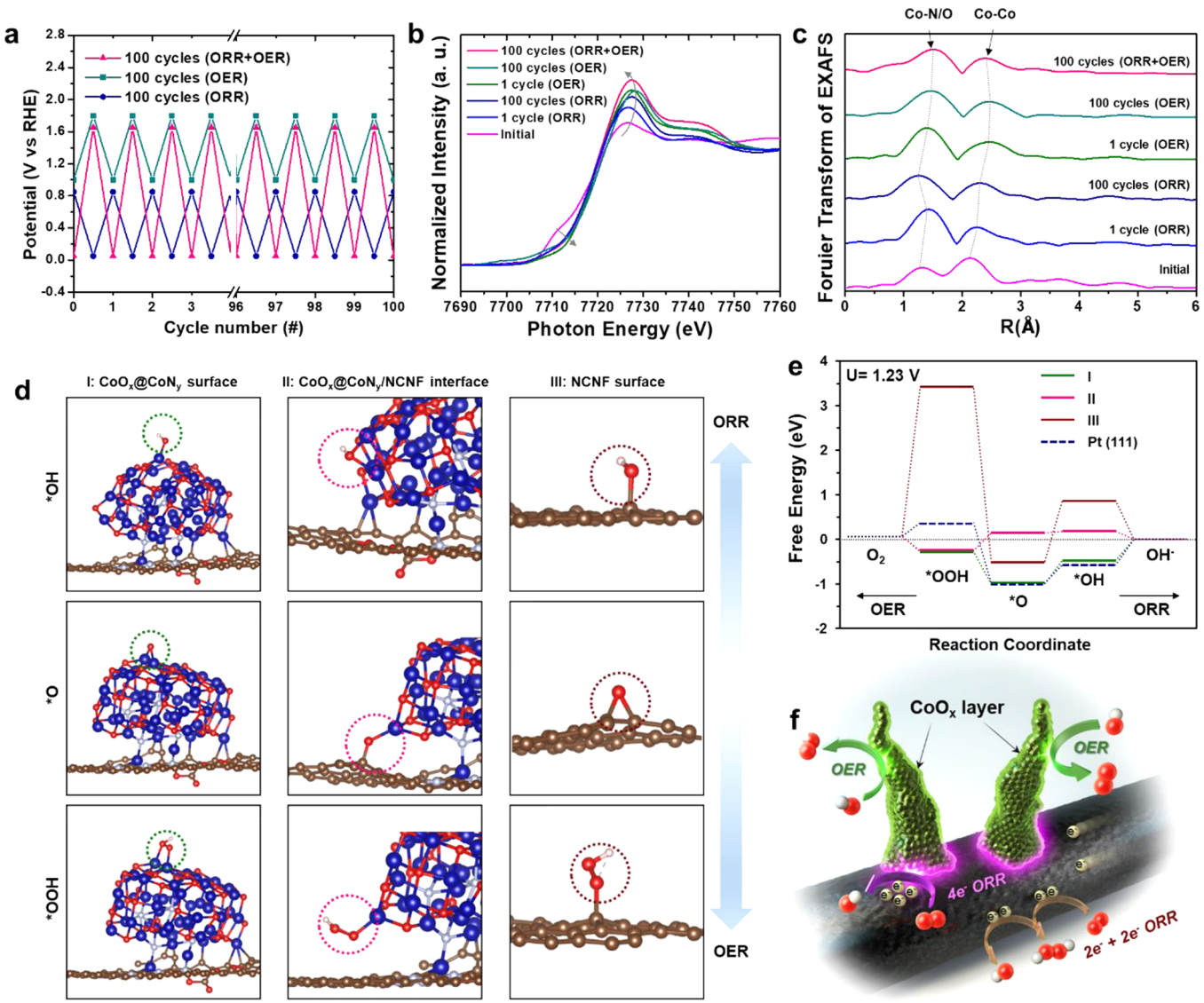

Figure 5. ***Ex situ*** **XAS analysis and DFT results of CoO_x@CoN_y/NCNF550 after ORR/OER cycling tests: (a) Potential sweep ranges in ORR, OER, and ORR + OER for cycling tests, (b) experimental Co *K*-edge XANES spectra, and (c) EXAFS of *K*-edge for the initial and after various cycling states of CoO_x@CoN_y/NCNF. DFT calculation for finding ORR/OER active sites. (d) Optimized geometrical structures of *OOH, *O, and *OH on the three different sites (I, CoO_x@CoN_y top surface; II, CoO_x@CoN_y and NCNF interface; III, pristine NCNF surface). The blue, red, gray, dark brown, and white spheres represent Co, O, N, C, and H, respectively. (e) ORR/OER free energy diagram at equilibrium potential (U = 1.23 V) on three different sites and the Pt(111) for comparison. (f) Proposed reaction scheme of CoO_x@CoN_y/NCNF toward ORR/OER.**

Two important aspects of a bifunctional catalyst are its outstanding durability and stability.[41] As shown in Figure 3g, the ORR durability of CoO_x@CoN_y/NCNF550 was compared with that of Pt/C using chronoamperometry at an ORR overpotential of 0.63 V. The ORR performance of commercial Pt/C dropped significantly when methanol was injected. This was due to the methanol poisoning of the active sites for the Pt-based catalyst.[42,43] In contrast, CoO_x@CoN_y/NCNF550 had exceptional retention with almost no reduction in its performance. Figure 3h illustrates the excellent OER stability of CoO_x@CoN_y/NCNF550. CoO_x@CoN_y/NCNF550 retained more than 95% of its initial OER performance capability, whereas commercial IrO_2 lost almost 20% of its initial current density after continuous OER operation for 18,000 s at an overpotential value of 0.37 V.

Next, we carried out electrochemical full-cell measurements in various applications, *i.e.*, an alkaline membrane fuel cell (AMFC), a water electrolyzer (WE), and a zinc−air battery (ZAB), to verify the practical value of the developed catalyst (CoO_x@CoN_y/NCNF550). As depicted in Figure 4a−c, the CoO_x@CoN_y/NCNF550 catalysts were utilized in the electrode materials (marked by pink dots) of the AMFC, WE, and ZAB systems (details are included in the Experimental Section) for ORR, for OER, and for both ORR and OER, respectively. The CoO_x@CoN_y/NCNF550-catalyst-coated MEA exhibited high electrochemical ORR performance in AMFC (Figure 4d),[41] with a considerable power density (~80 mW cm^{-2}) of 177.2 mA cm^{-2}. In addition, CoO_x@CoN_y/NCNF550-coated MEA delivered stable operating voltage (~0.6 V) during a chronopotentiometric test at 100 mA cm^{-2} for 60 h (Figure 4e).

Furthermore, the CoO_x@CoN_y/NCNF550-coated MEA exhibited high activity and stability in WE cells. As shown in Figure 4f, the OER current occurred with a low overpotential was achieved and maintained after a 50 h stability test. There

https://doi.org/10.1021/acsnano.0c09905
ACS Nano 2021, 15, 11218−11230

were no significant changes in the cell voltage during the chronopotentiometric stability test conducted here at 100 mA cm^{-2} for 50 h (Figure 4g). These results indicate that the ORR and OER active sites can be sustained under a continuous bias condition in actual MEA applications.

Finally, a rechargeable aqueous ZAB was assembled to demonstrate the bifunctional activity of the CoO_x@CoN_y/NCNF550 catalyst.[17] Figure 4h presents the galvanostatic discharge and charge curves of CoO_x@CoN_y/NCNF550 and "Pt/C + IrO_2" mixed cathodes at a current density of 10 mA cm^{-2} with a limited capacity of 1.667 mAh cm^{-2}. The initial overpotential gaps between the discharge and charge are 0.94 and 1.28 V for CoO_x@CoN_y/NCNF550 and Pt/C + IrO_2, respectively. The small overpotential gap is attributed to the high ORR and OER catalytic activity levels of CoO_x@CoN_y/NCNF550 during discharge and charge states in the ZAB. More importantly, the CoO_x@CoN_y/NCNF500 cathode delivered stable discharge/charge cyclic performance in the ZAB for more than 50 h (>150 cycles) with lower overpotentials compared to the mixture (Pt/C + RuO_2) reference electrode that became unstable within 36 h (Figure 4i). This clearly demonstrates that the ORR and OER active sites are preserved at the repeated bias potentials.

To assess the local structural changes in CoO_x@CoN_y/NCNF550 during the electrochemical reactions, we carried out potential sweeps in three different regions covering the ORR (0.85−0.05 V), OER (1.00−1.80 V), and ORR and the OER mixed (ORR + OER, 0.05−1.65 V) ranges for 100 cycles in all cases (Figure 5a). The potential sweep rate was maintained at 20 mV s^{-1}, and O_2 gas was purged such that ORR and/or OER occurred during the cyclic potential sweep. Then, we conducted an *ex situ* X-ray absorption spectroscopy analysis of CoO_x@CoN_y/NCNF550 in the initial state, after the first cycle, and after 100 cycles in the ORR, OER, and ORR + OER regions in each case.

Figure 5b presents the Co *K*-edge X-ray absorption near-edge structure spectra of CoO_x@CoN_y/NCNF550 from the initial state through the aforementioned prolonged potential cycles. After the first ORR and OER, the pre-edge shift in the positive direction indicates that partial oxidation occurred in the Co_4N nanorods, despite the fact that they naturally formed a thin oxide layer. More importantly, an increase in the white-line area was observed after the cycling tests, implying an increase in the flexibility in the d-band electron filling caused by the enhancement of the delocalized electron density.[27,44] This indicates that additional amounts of electrons in the CoO_x layer can more freely participate in the electrochemical reactions.

Figure 5c presents the modulation of the local structure of CoO_x@CoN_y/NCNF550 as characterized by the extended X-ray absorption fine-structure spectra. The overall shapes of the EXAFS spectra were preserved even when the intensity of the Co−N/O peaks became lower than it was during the initial cycles after continuing with the two alternative reactions. The reversible changes in the atomic bond distances of Co−N/O and Co−Co are denoted by the black dashed lines; these changes indicate good structural flexibility of CoO_x@CoN_y/NCNF550 during the repeated cycling tests. This is a crucial factor related to the reversibility of CoO_x@CoN_y/NCNF550 toward the ORR and OER, as demonstrated by its bifunctional activity in the ZAB (Figure 4i). It should be noted that the initial states of the heterogeneous catalytic structure were modulated after the electrochemical reactions. Furthermore, the preservation of catalytic sites with some structural flexibility is very important, especially in bifunctional catalysis.

To clarify the ORR/OER active sites of our catalyst, we calculated the adsorption energies of ORR/OER intermediates at different sites. Figure S15 presents the model structure, which has three clearly distinguishable positions (CoO_x@CoN_y surface, CoO_x@CoN_y/NCNF interface, and pristine NCNF surface) for adsorption. Consistent with previous studies, we assumed an associative mechanism that proceeds through *OOH, *O, and *OH (the asterisk denotes the adsorption site), and OER in reverse.[45,46] Figure S16 presents standard free energy diagrams of the CoO_x@CoN_y top surface, CoO_x@CoN_y/NCNF interface, and NCNF surface for the ORR/OER. Figure 5e and Table S3 present representative free energy diagrams of the equilibrium potential (U_{RHE}^0 = 1.23 V) as well as the calculated free energy barriers and onset potentials for the ORR/OER.

With regard to the ORR, the large value of ΔG_{*OOH} on the NCNF surface indicates that the *OOH on NCNF is so unstable that the reduction from O_2 to *OOH is energetically unfavorable. In contrast, on the CoO_x@CoN_y surface and the CoO_x@CoN_y/NCNF interface, the first step of the O_2 reduction to *OOH is exothermic. It has been reported that the C atoms close to doped N are readily acceptable adsorption sites for ORR/OER intermediates.[47,48] However, in our case they tended to be preferentially occupied by hydrothermally grown CoO_x@CoN_y nanorods.

In the second step of the ORR, all positions except the CoO_x@CoN_y/NCNF interface were endothermic. This was due to the weaker Co−O−C bonding caused by *OOH protonation at the CoO_x@CoN_y/NCNF interface as compared to Co−O−OH bonding. For both the ORR and OER, the ideal thermodynamic free energy change of the intermediates ($|\Delta G_{*OOH}|$, $|\Delta G_{*O}|$, and $|\Delta G_{*OH}|$) should be zero, indicating that no energy would be wasted to activate the reactions.[19]

The third and fourth steps of the ORR on the CoO_x@CoN_y/NCNF interfaces had almost no barrier. Moreover, it is presumable in the design that the reduction of intermediates at the rim sites can also be accelerated due to the rapid injection of charges from the adjacent NCNF. Meanwhile, the adsorption energies of *O and *OH on the CoO_x@CoN_y surface are similar to that of the (111) plane of the state-of-the-art Pt catalyst. Despite the fact that CoO_x@CoN_y is energetically favorable toward the ORR, the sole use of CoO_x@CoN_y nanorods led to an inferior ORR outcome. We suspect that the ORR is highly susceptible to the charge transfer such that the polycrystalline nature of the CoO_x@CoN_y nanorods, several micrometers long, may limit their ORR activity.

With regard to the OER, a considerable barrier ($|\Delta G_{*OOH}|$ = 3.93 V) occurred on the pristine NCNF surfaces. In contrast, both the CoO_x@CoN_y surface and the CoO_x@CoN_y/NCNF interface had relatively small barriers ($|\Delta G_{*OOH}|$ = 0.72 V and $|\Delta G_{O2}|$ = 0.31 V for the CoO_x@CoN_y surface and CoO_x@CoN_y/NCNF interface, respectively), indicating that CoO_x@CoN_y/NCNF has numerous active sites for the OER. Overall, the DFT calculations and experimental results were in good agreement, suggesting that the bifunctional ORR/OER activity was successfully enhanced by the synergistic coupling of CoO_x@CoN_y and NCNF.

On the basis of the experimental data and computational deductions, we confirmed that the CoO_x@CoN_y nanorods and NCNF were synergistically combined to address both ORR and OER. As described in Figure 5f, only the NCNF exhibited poor

https://doi.org/10.1021/acsnano.0c09905
ACS Nano 2021, 15, 11218−11230

ORR activity, undergoing a $2e^-$ transfer. In contrast, the interfacial rim sites between the CoO_x@CoN_y and NCNF facilitated the ORR with moderate adsorption of intermediates as well as a rapid charge injection. Meanwhile, the oxidized layers on the Co_4N nanorods provided efficient OER active sites with enhanced d-band vacancies of Co atoms.

CONCLUSIONS

In summary, we prepared CoO_x@CoN_y nanorod-anchored NCNF as a bifunctional hybrid catalyst and carried out various electrochemical measurements to determine their ORR and OER properties and durability in an alkaline solution. The outstanding ORR and OER activity and exceptional durability of the CoO_x@CoN_y/NCNF hybrid were confirmed by various half-cell measurements and full-cell applications (AMFC, WE, and ZAB). In addition to *ex situ* characterization and DFT calculations, we established that (i) the hierarchically assembled CoO_x@CoN_y/NCNF hybrid provides numerous accessible reaction sites especially for the OER; (ii) the synergistic coupling of the CoO_x@CoN_y/NCNF generates new ORR active rim sites and efficient charge transport channels, activating all of the catalytic sites; and (iii) the separate ORR and OER active sites were continuously activated and effectively sustained without mutual interference during prolonged reversible cycle tests. We believe that our findings can facilitate the design of highly efficient and durable heterogeneous bifunctional catalysts.

EXPERIMENTAL SECTION

Synthesis of Carbon Nanofiber. To synthesize the electrospun carbon nanofiber, 1 g of polyacrylonitrile (PAN, MW = 150,000 g mol^{-1}, Sigma-Aldrich) was dissolved in 6 g of *N*,*N*-dimethylformamide (DMF, Sigma-Aldrich) under vigorous stirring at 80 °C for 6 h. The PAN/DMF solution was transferred into the syringe, and a 25-gauge needle was capped on the syringe tip. A high voltage of 12.5 kV was applied between the needle and the stainless steel collector, which were separated by a distance of 15 cm. Then the elongated PAN was continuously fed from the needle to the collector at a feed rate of 15 μL min^{-1}. The electrospun PAN fiber was stabilized first at 250 °C for 2 h in the air followed by carbonization at 900 °C for 2 h in an Ar-filled tube furnace. The resultant sample was designated NCNF.

Preparation of CoO_x@CoN_y/NCNFs, CoO_x/NCNF550, and CoO_x@CoN_y550. The CoO_x@CoN_y/NCNF series were prepared using a simple hydrothermal method and subsequent nitridation process as reported in an earlier work.[25] In order to give the NCNF hydrophilic features, a piece of NCNF was placed in a dopamine solution using methanol (2 mg mL^{-1} of dopamine hydrochloride (98%, Sigma-Aldrich) and a 0.1 M Tris buffer solution (pH 8.5) as cosolvents (CH_3OH:buffer = 1:1 (v/v)) to self-polymerize the dopamine on the surface of NCNF overnight.[26] After polymerization, the dopamine solution changed from pale to dark brown, indicating that self-polymerization of dopamine had occurred. After removing the residual solvent and floating polydopamine (PD) particles, the PD-treated NCNF was washed with DI water several times and then dried in a convection oven at 50 °C. Next, 0.291 g of cobalt(II) nitrate hexahydrate ($Co(NO_3)_2{\cdot}6H_2O$, Sigma-Aldrich), 0.093 g of ammonium fluoride (NH_4F, Sigma-Aldrich), and 0.3 g of urea ($CO(NH_2)_2$, Sigma-Aldrich) were dissolved in 20 mL of DI water, and then the cleaned NCNF was soaked in the mixed solution with stirring at 100 rpm for over 2 h. The mixed solution and NCNF were transferred to a 100 mL Teflon-lined autoclave and kept at 120 °C for 6 h (5 °C min^{-1}). After cooling to room temperature, the cobalt fluoride hydroxide coated NCNF (Co(OH)F/NCNF) was taken out and rinsed with DI water and EtOH several times and dried in a convection oven at 50 °C. Finally, the Co(OH)F/NCNF was calcined at 550 °C for 2 h (5 °C min^{-1}) in an Ar-filled tube furnace with ammonia gas (NH_3) at a flow rate of 100 sccm. After cooling, the obtained product was collected and designated CoO_x@CoN_y/NCNF550. As comparative samples, CoO_x@CoN_y/NCNF450 and CoO_x@CoN_y/NCNF650 were similarly prepared with nitridation temperatures of 450 and 650 °C for 2 h, respectively. The CoN_x/NCNF550 was prepared by calcination at 550 °C for 2 h in air instead of nitridation. For CoO_x@CoN_y550 without NCNF, the Co(OH)F was grown on a piece of silicon wafer instead of NCNF during the hydrothermal reaction, and subsequently peeled off the Si wafer. The obtained Co(OH)F powders were then calcined at 550 °C with an Ar purged furnace with NH_3 gas.

Material Characterization. The microstructures of the prepared samples were observed using a scanning electron microscope (SEM, Philips, USA) and Tecnai TF30 S-Twin transmission electron microscope (TEM, FEI Co., USA). The crystalline structure of the samples was analyzed by powder X-ray diffractometer (XRD, D/MAX-2500, RIGAKU Co., Japan), and the surface chemical state was investigated by X-ray photoelectron spectroscopy (XPS, Thermo VG Scientific Co., U.K.). Thermogravimetric analysis (TGA) data were collected on a TA Instruments Q50, which was heated from 25 to 900 °C at a heating rate of 10 °C min^{-1} in N_2/O_2 (7:3 (v/v)) atmosphere. To analyze local atomic structure and relative bond lengths with respect to absorbing atoms, EXAFS measurements were performed at the hard X-ray 1D XAS KIST-PAL beamline,[49] Pohang accelerator laboratory, operating at 3.0 GeV with a maximum storage current of 360 mA. EXAFS data were processed using ATHENA and simulated by ARTEMIS.[50]

Electrochemical Half-Cell Test. All electrochemical measurements were performed using a conventional three-electrode rotating ring disk system using an AutoLab PGSTAT 302N potentiostat. The catalysts loaded glassy carbon electrode (GCE; geometric area, 0.196 cm^2) was used as a working electrode, and a saturated calomel electrode (SCE) and Pt wire were used as the reference electrode and counter electrode, respectively. For electrochemical three-electrode tests, all freestanding catalyst samples were thoroughly ground and then treated sonication with solvents. For the working electrodes, 15 mg of CoO_x@CoN_y/NCNF samples were mixed into 50 μL of Nafion solution (5 wt %, Sigma-Aldrich) added to a 500 μL isopropyl alcohol (IPA) solution. After vigorous mixing with ultrasonication, 15 μL of the homogeneous catalyst ink was transferred onto the GCE (loading amount of catalysts was 2.087 mg cm^{-2}) and dried at 50 °C for the measurements. The dried electrode was then transferred to the rotating disk electrode (RDE) setup, and O_2 saturated 0.1 M KOH aqueous solution was used as the electrolyte for both the ORR and OER measurements. All polarization curves were obtained at a scan rate of 5 mV s^{-1} for 1600 rpm, and the measured potentials were calibrated to a reversible hydrogen electrode (RHE) potential using Nernst equation: $E_{RHE} = E_{SCE} + E^0_{SCE} + 0.059pH$ ($E^0_{SCE} = 0.244$ V). To examine the electron-transfer kinetics and H_2O_2 selectivity, rotating ring disk electrode (RRDE; geometric area of ring and disk electrodes is 0.247 cm^2) voltammetry was performed using an AFMSRCE advanced electrochemical system (Pine Instrument Co., USA).

Fabrication of MEA and Electrochemical Alkaline Membrane Fuel-Cell Test. A membrane electrode assembly (MEA) for use in a fuel-cell setup was prepared by a catalyst-coated membrane method using a commercial anion exchange membrane (Tokuyama, A-201). For the electrodes, a commercial Pt/C catalyst (46.5 wt %, Tanaka Co.) with 0.2 mg cm^{-2} Pt loading was applied at the anode, and CoO_x@CoN_y/NCNF catalysts with 1.26 mg cm^{-2} were applied at the cathode. Each catalyst was dispersed in a mixture of isopropyl alcohol and ionomer (AS-4, Tokuyama, 5 wt %) with a loading 30 wt % of catalysts to prepare the homogeneous ink. The resulting MEA was loaded into a 1 cm^2 cell assembly. Carbon paper (39BC) was used as a gas diffusion layer (GDL) at the anode and cathode. The performance of the MEA in a fuel-cell device was examined using a test system at 60 °C with H_2 and O_2.

Fabrication of Electrode and Water Electrolysis Tests. The 1 cm^2 MEA for the single-cell electrolysis test was prepared by a catalyst-coated on membrane (CCM) method with A201 (Tokuyama) membrane. Titanium paper (Toray, 250 μm, anode) and carbon paper (39BC, cathode) were used as a gas diffusion layer (GDL) at the

https://doi.org/10.1021/acsnano.0c09905
ACS Nano 2021, 15, 11218−11230

anode and cathode, respectively. The catalyst ink slurry, consisting of catalysts, the ionomer (AS-4, Tokuyama, 5 wt %), isopropyl alcohol and DI water, was homogenized in an ultrasonic bath for 1 h. Each electrode was fabricated by spray-coating 8 mg cm^{-2} of the synthesized CoO_x@CoN_y/NCNF catalysts on the membrane for the anode and 3 mg cm^{-2} Pt/C (Pt 46.5 wt %, Tanaka Co.) for the cathode. A 0.5 M KOH solution was fed at 15 mL min^{-1} on the anode side during the test. The IV curves were obtained by cyclic voltammetry from 1.4 to 2.2 V at the 20 mV s^{-1} scan rate with a high-current potentiostat (HCP-803, Bio-Logic). The stability test of the CoO_x@CoN_y/NCNF catalysts was run at a constant current density of 100 mA cm^{-2} for 60 h under the same conditions.

Zn−Air Battery Test. The electrochemical performance of Zn−air battery (ZAB) cells were evaluated using a home-built two-electrode cell.[17] Pure Zn foil (Alfa Aesar, 0.62 mm in thickness, 1 × 3 cm^2 area, 99.9%, USA) was used as a counter electrode. The freestanding CoO_x@CoN_y/NCNF paper was directly used as a bifunctional ZAB cathode. An aqueous liquid electrolyte (6 M KOH solution with 0.2 M zinc acetate) was employed to let ions pass through. The reference electrode in the ZAB was composed of commercial Pt/C (20 wt % Pt) and RuO_2 (1:1 (w/w)) with a total mass loading 1 mg ± 0.1 cm^{-2}. Ni mesh was utilized as an electrically conductive current collector. A poly(tetrafluoroethylene) (PTFE) membrane at the cathode side functioned as a gas diffusion layer as well as a selective membrane for O_2 gas from ambient air.

Computational Details. The calculations reported herein were performed on the basis of spin-polarized density functional theory (DFT) within the Perdew−Burke−Ernzerhof (PBE) as implemented in the Vienna *ab initio* simulation package (VASP).[51,52] The projector augmented wave (PAW) method using a plane wave basis set was implemented to describe the interaction between core and valence electrons. An energy cutoff of 400 eV was used for the plane wave expansion of the electronic eigenfunctions.[53] For the Brillouin zone integration, we accepted (12 × 12 × 12), (16 × 16 × 16), (8 × 8 × 1), and (2 × 2 × 1) Monkhorst−Pack mesh of *k*-points to determine the equilibrium geometries and total energies of bulk CoO (*Fm*3*m*), Co_4N (*Pm*3*m*), pristine graphene ($P6_3/mmc$), and CoO_x@CoN_y/NCNF, respectively.[54] The calculated equilibrium lattice constants for the bulk CoO and Co_4N were and 4.20 and 3.71 Å, which were similar to the experimental results of 4.26 and 3.74 Å, respectively.[55] We adopted the "DFT + U" method to partially circumvent the well-known self-interaction error, which affects the electronic structure of semiconducting oxides calculated with GGA.[56−58] In this work, we empirically set this parameter to 3.3 for Co, which ensures a good qualitative description of the structure and electronic properties of the cobalt oxides. In the CoO_x@CoN_y/NCNF model, a Co_4N nanocluster was surrounded by rocksalt-structured CoO except for the −*z* direction, to form a sheath−core geometry of Co_4N−CoO. We designed the geometry of the turbostratic NCNF to follow our previous research, which includes vacancies, and doped N and O atoms to match the experimental results.[17] On the basis of the experimental results, the CoO_x@CoN_y and NCNF models were combined at the vacant sites of the NCNF at a distance of 3 Å in the *z* direction. This CoO_x@CoN_y/NCNF model was fully relaxed using the conjugate gradient method until the residual forces on all of the constituent atoms became smaller than 0.05 eV/Å. The adsorption energies (ΔE_{ads}) of the ORR/OER intermediates were calculated using the following equation;

$$\Delta E_{ads}(X) = E_{X*} - (E_X + E_*)$$

where E_{X*}, E_X, and E_* are the total energies of the X-adsorbed slab, isolated X species, and the clean surface, respectively. X denotes O, OH, and OOH. To calculate the Gibbs free energy of the electrocatalytic ORR, we followed Nørskov's procedures.[58]

ASSOCIATED CONTENT

Supporting Information

The Supporting Information is available free of charge at https://pubs.acs.org/doi/10.1021/acsnano.0c09905.

Supplementary data including XPS, TGA, SEM, EDS, SAED, and additional electrochemical data, *etc.*, and related text (PDF)

AUTHOR INFORMATION

Corresponding Authors

Il-Doo Kim − *Department of Materials Science and Engineering, Korea Advanced Institute of Science and Technology (KAIST), Daejeon 34141, Republic of Korea;* orcid.org/0000-0002-9970-2218; Email: idkim@kaist.ac.kr

Jin Young Kim − *Center for Hydrogen & Fuel Cell Research, Korea Institute of Science and Technology (KIST), Seoul 02792, Republic of Korea;* orcid.org/0000-0003-4822-3804; Email: jinykim@kist.re.kr

Authors

Ki Ro Yoon − *Advanced Textile R&D Department, Korea Institute of Industrial Technology, Ansan-si, Gyeonggi-do 15588, Republic of Korea; Center for Hydrogen & Fuel Cell Research, Korea Institute of Science and Technology (KIST), Seoul 02792, Republic of Korea;* orcid.org/0000-0003-3532-7911

Chang-Kyu Hwang − *Advanced Textile R&D Department, Korea Institute of Industrial Technology, Ansan-si, Gyeonggi-do 15588, Republic of Korea; Center for Hydrogen & Fuel Cell Research, Korea Institute of Science and Technology (KIST), Seoul 02792, Republic of Korea; Department of Electrical Engineering, Korea University, Seoul 02841, Republic of Korea*

Seung-hoon Kim − *Center for Hydrogen & Fuel Cell Research, Korea Institute of Science and Technology (KIST), Seoul 02792, Republic of Korea; Green School (Graduate School of Energy & Environment), Korea University, Seoul 02841, Republic of Korea*

Ji-Won Jung − *School of Materials Science and Engineering, University of Ulsan, Ulsan 44776, Republic of Korea*

Ji Eon Chae − *Center for Hydrogen & Fuel Cell Research, Korea Institute of Science and Technology (KIST), Seoul 02792, Republic of Korea*

Jun Kim − *Center for Hydrogen & Fuel Cell Research, Korea Institute of Science and Technology (KIST), Seoul 02792, Republic of Korea*

Kyung Ah Lee − *Center for Hydrogen & Fuel Cell Research, Korea Institute of Science and Technology (KIST), Seoul 02792, Republic of Korea*

Ahyoun Lim − *Center for Hydrogen & Fuel Cell Research, Korea Institute of Science and Technology (KIST), Seoul 02792, Republic of Korea*

Su-Ho Cho − *Department of Materials Science and Engineering, Korea Advanced Institute of Science and Technology (KAIST), Daejeon 34141, Republic of Korea*

Jitendra Pal Singh − *Advanced Analysis Center, Korea Institute of Science and Technology (KIST), Seoul 02792, Republic of Korea;* orcid.org/0000-0001-8500-8236

Jong Min Kim − *Center for Hydrogen & Fuel Cell Research, Korea Institute of Science and Technology (KIST), Seoul 02792, Republic of Korea*

Kihyun Shin − *Department of Chemistry, and the Oden Institute for Computational Engineering and Sciences, University of Texas at Austin, Austin, Texas 78712, United States;* orcid.org/0000-0002-1748-8773

Byung Moo Moon − *Department of Electrical Engineering, Korea University, Seoul 02841, Republic of Korea*

Hyun S. Park − *Center for Hydrogen & Fuel Cell Research, Korea Institute of Science and Technology (KIST), Seoul 02792, Republic of Korea;* orcid.org/0000-0002-7960-9729

Hyoung-Juhn Kim − *Center for Hydrogen & Fuel Cell Research, Korea Institute of Science and Technology (KIST), Seoul 02792, Republic of Korea*

Keun Hwa Chae − *Advanced Analysis Center, Korea Institute of Science and Technology (KIST), Seoul 02792, Republic of Korea;* orcid.org/0000-0003-3894-670X

Hyung Chul Ham − *Department of Chemistry and Chemical Engineering, Education and Research Center for Smart Energy and Materials, Inha University, Incheon 22212, Republic of Korea;* orcid.org/0000-0003-0850-584X

Complete contact information is available at: https://pubs.acs.org/10.1021/acsnano.0c09905

Author Contributions

¶K.R.Y., C.-K.H., and S.-h.K. contributed equally to this work.

Notes

The authors declare no competing financial interest.

ACKNOWLEDGMENTS

This work was supported by the National Research Foundation of Korea (NRF) grant funded by the Korean Government (MSIT; No. 2019R1F1A1044908). This study has been conducted with the support of the Korea Institute of Industrial Technology (Grant No. kitech JA-20-0001) and the Gyeongi-Do Technology Development Program (Grant No. kitech IZ-20-0004) as "Development of smart textronic products based on electronic fibers and textiles". This work was also supported by the National Research Foundation of Korea (NRF) grant of the Korean Government (NRF-2019M3D1A2104101). This work was supported by the KIST Institutional Program (2E31002). This research was supported by the Hydrogen Energy Innovation Technology Development Program of the National Research Foundation of Korea (NRF) funded by the Korean government (Ministry of Science and ICT(MSIT)) (No. 2019M3E6A1063674).

REFERENCES

(1) Ge, X.; Sumboja, A.; Wuu, D.; An, T.; Li, B.; Goh, F. W. T.; Hor, T. S. A.; Zong, Y.; Liu, Z. Oxygen Reduction in Alkaline Media: From Mechanisms to Recent Advances of Catalysts. *ACS Catal.* **2015**, *5* (8), 4643−4667.

(2) Davari, E.; Ivey, D. G. Bifunctional Electrocatalysts for Zn−Air Batteries. *Sustain. Energy Fuels* **2018**, *2* (1), 39−67.

(3) Wang, Z. L.; Xu, D.; Xu, J. J.; Zhang, X. B. Oxygen Electrocatalysts in Metal-Air Batteries: from Aqueous to Nonaqueous Electrolytes. *Chem. Soc. Rev.* **2014**, *43* (22), 7746−7786.

(4) Fabbri, E.; Habereder, A.; Waltar, K.; Kötz, R.; Schmidt, T. J. Developments and Perspectives of Oxide-Based Catalysts for the Oxygen Evolution Reaction. *Catal. Sci. Technol.* **2014**, *4* (11), 3800−3821.

(5) Khalid, M.; Honorato, A. M. B.; Varela, H.; Dai, L. Multifunctional Electrocatalysts Derived from Conducting Polymer and Metal Organic Framework Complexes. *Nano Energy* **2018**, *45*, 127−135.

(6) Li, R.; Wei, Z.; Gou, X. Nitrogen and Phosphorus Dual-Doped Graphene/Carbon Nanosheets as Bifunctional Electrocatalysts for Oxygen Reduction and Evolution. *ACS Catal.* **2015**, *5* (7), 4133−4142.

(7) Yang, M.-Q.; Wang, J.; Wu, H.; Ho, G. W. Noble Metal-Free Nanocatalysts with Vacancies for Electrochemical Water Splitting. *Small* **2018**, *14*, 1703323.

(8) Liu, X.; Dai, L. Carbon-Based Metal-Free Catalysts. *Nat. Rev. Mater.* **2016**, *1* (11), 16064.

(9) Liu, K.; Zhong, H.; Meng, F.; Zhang, X.; Yan, J.; Jiang, Q. Recent Advances in Metal−Nitrogen−Carbon Catalysts for Electrochemical Water Splitting. *Mater. Chem. Front.* **2017**, *1*, 2155−2173.

(10) Lin, L.; Zhu, Q.; Xu, A. W. Noble-Metal-Free Fe-N/C Catalyst for Highly Efficient Oxygen Reduction Reaction under Both Alkaline and Acidic Conditions. *J. Am. Chem. Soc.* **2014**, *136* (31), 11027−33.

(11) Bezerra, C. W. B.; Zhang, L.; Lee, K.; Liu, H.; Marques, A. L. B.; Marques, E. P.; Wang, H.; Zhang, J. A Review of Fe−N/C and Co−N/C Catalysts for the Oxygen Reduction Reaction. *Electrochim. Acta* **2008**, *53* (15), 4937−4951.

(12) Lai, L.; Potts, J. R.; Zhan, D.; Wang, L.; Poh, C. K.; Tang, C.; Gong, H.; Shen, Z.; Lin, J.; Ruoff, R. S. Exploration of the Active Center Structure of Nitrogen-Doped Graphene-Based Catalysts for Oxygen Reduction Reaction. *Energy Environ. Sci.* **2012**, *5* (7), 7936−7942.

(13) Zhang, C.; Wang, B.; Shen, X.; Liu, J.; Kong, X.; Chuang, S. S. C.; Yang, D.; Dong, A.; Peng, Z. A Nitrogen-Doped Ordered Mesoporous Carbon/Graphene Framework as Bifunctional Electrocatalyst for Oxygen Reduction and Evolution Reactions. *Nano Energy* **2016**, *30*, 503−510.

(14) Li, S. S.; Cong, H. P.; Wang, P.; Yu, S. H. Flexible Nitrogen-Doped Graphene/Carbon Nanotube/Co_3O_4 Paper and Its Oxygen Reduction Activity. *Nanoscale* **2014**, *6* (13), 7534−7541.

(15) Chai, G.-L.; Qiu, K.; Qiao, M.; Titirici, M.-M.; Shang, C.; Guo, Z. Active Sites Engineering Leads to Exceptional ORR and OER Bifunctionality in P,N Co-Doped Graphene Frameworks. *Energy Environ. Sci.* **2017**, *10* (5), 1186−1195.

(16) Zhang, J.; Zhao, Z.; Xia, Z.; Dai, L. A Metal-Free Bifunctional Electrocatalyst for Oxygen Reduction and Oxygen Evolution Reactions. *Nat. Nanotechnol.* **2015**, *10* (5), 444−452.

(17) Yoon, K. R.; Choi, J.; Cho, S.-H.; Jung, J.-W.; Kim, C.; Cheong, J. Y.; Kim, I.-D. Facile Preparation of Efficient Electrocatalysts for Oxygen Reduction Reaction: One-Dimensional Meso/Macroporous Cobalt and Nitrogen Co-Doped Carbon Nanofibers. *J. Power Sources* **2018**, *380*, 174−184.

(18) Masa, J.; Xia, W.; Sinev, I.; Zhao, A.; Sun, Z.; Grutzke, S.; Weide, P.; Muhler, M.; Schuhmann, W. Mn_xO_y/NC and Co_xO_y/NC Nanoparticles Embedded in a Nitrogen-Doped Carbon Matrix for High-Performance Bifunctional Oxygen Electrodes. *Angew. Chem., Int. Ed.* **2014**, *53* (32), 8508−8512.

(19) Ling, T.; Yan, D.-Y.; Jiao, Y.; Wang, H.; Zheng, Y.; Zheng, X.; Mao, J.; Du, X.-W.; Hu, Z.; Jaroniec, M.; Qiao, S.-Z. Engineering Surface Atomic Structure of Single-Crystal Cobalt (II) Oxide Nanorods for Superior Electrocatalysis. *Nat. Commun.* **2016**, *7* (1), 12876.

(20) Nam, G.; Son, Y.; Park, S. O.; Jeon, W. C.; Jang, H.; Park, J.; Chae, S.; Yoo, Y.; Ryu, J.; Kim, M. G.; Kwak, S. K.; Cho, J. A Ternary $Ni_{46}Co_{40}Fe_{14}$ Nanoalloy-Based Oxygen Electrocatalyst for Highly Efficient Rechargeable Zinc-Air Batteries. *Adv. Mater.* **2018**, *30* (46), No. 1803372.

(21) Jiang, G.; Jiang, N.; Zheng, N.; Chen, X.; Mao, J.; Ding, G.; Li, Y.; Sun, F.; Li, Y. MOF-Derived Porous Co_3O_4-NC Nanoflake Arrays on Carbon Fiber Cloth as Stable Hosts for Dendrite-Free Li Metal Anodes. *Energy Storage Mater.* **2019**, *23*, 181−189.

(22) Chen, Y. M.; Yu, L.; Lou, X. W. Hierarchical Tubular Structures Composed of Co_3O_4 Hollow Nanoparticles and Carbon Nanotubes for Lithium Storage. *Angew. Chem., Int. Ed.* **2016**, *55* (20), 5990−5993.

(23) Lee, H.; Kim, Y.-J.; Lee, D. J.; Song, J.; Lee, Y. M.; Kim, H.-T.; Park, J.-K. Directly Grown Co_3O_4 Nanowire Arrays on Ni-foam: Structural Effects of Carbon-Free and Binder-Free Cathodes for Lithium−Oxygen Batteries. *J. Mater. Chem. A* **2014**, *2* (30), 11891−11898.

(24) Liang, Y.; Li, Y.; Wang, H.; Zhou, J.; Wang, J.; Regier, T.; Dai, H. Co_3O_4 Nanocrystals on Graphene as a Synergistic Catalyst for Oxygen Reduction Reaction. *Nat. Mater.* **2011**, *10* (10), 780−786.

(25) Yoon, K. R.; Shin, K.; Park, J.; Cho, S. H.; Kim, C.; Jung, J. W.; Cheong, J. Y.; Byon, H. R.; Lee, H. M.; Kim, I. D. Brush-Like Cobalt Nitride Anchored Carbon Nanofiber Membrane: Current Collector-

Catalyst Integrated Cathode for Long Cycle Li-O_2 Batteries. *ACS Nano* **2018**, *12* (1), 128−139.
(26) Yoon, K. R.; Lee, K. A.; Jo, S.; Yook, S. H.; Lee, K. Y.; Kim, I.-D.; Kim, J. Y. Mussel-Inspired Polydopamine-Treated Reinforced Composite Membranes with Self-Supported CeO_x Radical Scavengers for Highly Stable PEM Fuel Cells. *Adv. Funct. Mater.* **2019**, *29*, 1806929.
(27) Chen, P.; Xu, K.; Fang, Z.; Tong, Y.; Wu, J.; Lu, X.; Peng, X.; Ding, H.; Wu, C.; Xie, Y. Metallic Co_4N Porous Nanowire Arrays Activated by Surface Oxidation as Electrocatalysts for the Oxygen Evolution Reaction. *Angew. Chem., Int. Ed.* **2015**, *54* (49), 14710−14714.
(28) Zhong, X.; Jiang, Y.; Chen, X.; Wang, L.; Zhuang, G.; Li, X.; Wang, J.-g. Integrating Cobalt Phosphide and Cobalt Nitride-Embedded Nitrogen-Rich Nanocarbons: High-Performance Bifunctional Electrocatalysts for Oxygen Reduction and Evolution. *J. Mater. Chem. A* **2016**, *4* (27), 10575−10584.
(29) Milad, I. K.; Smith, K. J.; Wong, P. C.; Mitchell, K. A. R. A Comparison of Bulk Metal Nitride Catalysts for Pyridine Hydrodenitrogenation. *Catal. Lett.* **1998**, *52*, 113−119.
(30) Yao, Z.; Zhu, A.; Chen, J.; Wang, X.; Au, C. T.; Shi, C. Synthesis, Characterization and Activity of Alumina-Supported Cobalt Nitride for NO Decomposition. *J. Solid State Chem.* **2007**, *180* (9), 2635−2640.
(31) Oda, K.; Yoshio, T.; Oda, K. Preparation of Co-N Films by RF-Sputtering. *J. Mater. Sci.* **1987**, *22*, 2729−2733.
(32) Chen, P.; Xu, K.; Tong, Y.; Li, X.; Tao, S.; Fang, Z.; Chu, W.; Wu, X.; Wu, C. Cobalt Nitrides as a Class of Metallic Electrocatalysts for the Oxygen Evolution Reaction. *Inorg. Chem. Front.* **2016**, *3* (2), 236−242.
(33) Gupta, R.; Pandey, N.; Tayal, A.; Gupta, M. Phase Formation, Thermal Stability and Magnetic Moment of Cobalt Nitride Thin Films. *AIP Adv.* **2015**, *5* (9), No. 097131.
(34) Zhao, X.; Ke, L.; Wang, C.-Z.; Ho, K.-M. Metastable Cobalt Nitride Structures with High Magnetic Anisotropy for Rare-Earth Free Magnets. *Phys. Chem. Chem. Phys.* **2016**, *18* (46), 31680−31690.
(35) Cho, S.-H.; Yoon, K. R.; Shin, K.; Jung, J.-W.; Kim, C.; Cheong, J. Y.; Youn, D.-Y.; Song, S. W.; Henkelman, G.; Kim, I.-D. Synergistic Coupling of Metallic Cobalt Nitride Nanofibers and IrO_x Nanoparticle Catalysts for Stable Oxygen Evolution. *Chem. Mater.* **2018**, *30* (17), 5941−5950.
(36) Meganathan, M. D.; Mao, S.; Huang, T.; Sun, G. Reduced Graphene Oxide Intercalated Co_2C or Co_4N Nanoparticles as an Efficient and Durable Fuel Cell Catalyst for Oxygen Reduction. *J. Mater. Chem. A* **2017**, *5* (6), 2972−2980.
(37) Jiang, H.; Gu, J.; Zheng, X.; Liu, M.; Qiu, X.; Wang, L.; Li, W.; Chen, Z.; Ji, X.; Li, J. Defect-Rich and Ultrathin N Doped Carbon Nanosheets as Advanced Trifunctional Metal-Free Electrocatalysts for the ORR, OER and HER. *Energy Environ. Sci.* **2019**, *12* (1), 322−333.
(38) Han, H.; Choi, H.; Mhin, S.; Hong, Y.-R.; Kim, K. M.; Kwon, J.; Ali, G.; Chung, K. Y.; Je, M.; Umh, H. N.; Lim, D.-H.; Davey, K.; Qiao, S.-Z.; Paik, U.; Song, T. Advantageous Crystalline−Amorphous Phase Boundary for Enhanced Electrochemical Water Oxidation. *Energy Environ. Sci.* **2019**, *12* (8), 2443−2454.
(39) Han, H.; Kim, K. M.; Choi, H.; Ali, G.; Chung, K. Y.; Hong, Y.-R.; Choi, J.; Kwon, J.; Lee, S. W.; Lee, J. W.; Ryu, J. H.; Song, T.; Mhin, S. Parallelized Reaction Pathway and Stronger Internal Band Bending by Partial Oxidation of Metal Sulfide−Graphene Composites: Important Factors of Synergistic Oxygen Evolution Reaction Enhancement. *ACS Catal.* **2018**, *8* (5), 4091−4102.
(40) Jeong, B.; Shin, D.; Choun, M.; Maurya, S.; Baik, J.; Mun, B. S.; Moon, S.-H.; Su, D.; Lee, J. Nitrogen-Deficient ORR Active Sites Formation by Iron-Assisted Water Vapor Activation of Electrospun Carbon Nanofibers. *J. Phys. Chem. C* **2016**, *120* (14), 7705−7714.
(41) Lee, K. J.; Shin, D. Y.; Byeon, A.; Lim, A.; Jo, Y. S.; Begley, A.; Lim, D. H.; Sung, Y. E.; Park, H. S.; Chae, K. H.; Nam, S. W.; Lee, K. Y.; Kim, J. Y. Hierarchical Cobalt-Nitride and -Oxide Co-Doped Porous Carbon Nanostructures for Highly Efficient and Durable Bifunctional Oxygen Reaction Electrocatalysts. *Nanoscale* **2017**, *9* (41), 15846−15855.
(42) Li, J.; Zhou, H.; Zhuo, H.; Wei, Z.; Zhuang, G.; Zhong, X.; Deng, S.; Li, X.; Wang, J. Oxygen Vacancies on TiO_2 Promoted the Activity and Stability of Supported Pd Nanoparticles for the Oxygen Reduction Reaction. *J. Mater. Chem. A* **2018**, *6*, 2264−2272.
(43) Oh, H.-S.; Lim, K. H.; Roh, B.; Hwang, I.; Kim, H. Corrosion Resistance and Sintering Effect of Carbon Supports in Polymer Electrolyte Membrane Fuel Cells. *Electrochim. Acta* **2009**, *54* (26), 6515−6521.
(44) Wang, Y.; Zhou, T.; Jiang, K.; Da, P.; Peng, Z.; Tang, J.; Kong, B.; Cai, W.-B.; Yang, Z.; Zheng, G. Reduced Mesoporous Co_3O_4 Nanowires as Efficient Water Oxidation Electrocatalysts and Supercapacitor Electrodes. *Adv. Energy Mater.* **2014**, *4* (16), 1400696.
(45) Fei, H.; Dong, J.; Feng, Y.; Allen, C. S.; Wan, C.; Volosskiy, B.; Li, M.; Zhao, Z.; Wang, Y.; Sun, H.; An, P.; Chen, W.; Guo, Z.; Lee, C.; Chen, D.; Shakir, I.; Liu, M.; Hu, T.; Li, Y.; Kirkland, A. I.; Duan, X.; Huang, Y. General Synthesis and Definitive Structural Identification of MN_4C_4 Single-Atom Catalysts with Tunable Electrocatalytic Activities. *Nat. Catal.* **2018**, *1* (1), 63−72.
(46) Guo, D.; Shibuya, R.; Akiba, C.; Saji, S.; Kondo, T.; Nakamura, J. Active Sites of Nitrogen-Doped Carbon Materials for Oxygen Reduction Reaction Clarified Using Model Catalysts. *Science* **2016**, *351* (6271), 361−365.
(47) Li, Y.; Zhou, W.; Wang, H.; Xie, L.; Liang, Y.; Wei, F.; Idrobo, J. C.; Pennycook, S. J.; Dai, H. An Oxygen Reduction Electrocatalyst Based on Carbon Nanotube-Graphene Complexes. *Nat. Nanotechnol.* **2012**, *7* (6), 394−400.
(48) Gong, K.; Du, F.; Xia, Z.; Durstock, M.; Dai, L. Nitrogen-Doped Carbon Nanotube Arrays with High Electrocatalytic Activity for Oxygen Reduction. *Science* **2009**, *323*, 760−764.
(49) Lee, I. J.; Yu, C. J.; Yun, Y. D.; Lee, C. S.; Seo, I. D.; Kim, H. Y.; Lee, W. W.; Chae, K. H. Note: Construction of X-Ray Scattering and X-Ray Absorption Fine Structure Beamline at the Pohang Light Source. *Rev. Sci. Instrum.* **2010**, *81* (2), No. 026103.
(50) Ravel, B.; Newville, M. ATHENA, ARTEMIS, HEPHAESTUS: Data Analysis for X-Ray Absorption Spectroscopy Using IFEFFIT. *J. Synchrotron Radiat.* **2005**, *12* (4), 537−541.
(51) Hammer, B.; Hansen, L. B.; Nørskov, J. K. Improved Adsorption Energetics within Density-Functional Theory Using Revised Perdew-Burke-Ernzerhof Functionals. *Phys. Rev. B: Condens. Matter Mater. Phys.* **1999**, *59*, 7413−7421.
(52) Kresse, G.; Furthmuller, J. Efficient Iterative Schemes for *ab Initio* Total-Energy Calculations Using a Plane-Wave Basis Set. *Phys. Rev. B: Condens. Matter Mater. Phys.* **1996**, *54* (16), 11169.
(53) Blöchl, P. E. Projector Augmented-Wave Method. *Phys. Rev. B: Condens. Matter Mater. Phys.* **1994**, *50* (24), 17953−17979.
(54) Blochl, P. E.; Jepsen, O.; Andersen, O. K. Improved Tetrahedron Method for Brillouin-Zone Integrations. *Phys. Rev. B: Condens. Matter Mater. Phys.* **1994**, *49*, 16223−16233.
(55) Navrotsky, A. Thermodynamic Relations among Olivine, Spinel, and Phenacite Structures in Silicates and Germanates: I. Volume Relations and the Systems NiO-MgO-GeO_2 and CoO-MgO-GeO_2. *J. Solid State Chem.* **1973**, *6* (1), 21−41.
(56) Anisimov, V. I.; Zaanen, J.; Andersen, O. K. Band Theory and Mott Insulators: Hubbard U Instead of Stoner I. *Phys. Rev. B: Condens. Matter Mater. Phys.* **1991**, *44*, 943−954.
(57) Dudarev, S. L.; Botton, G. A.; Savrasov, S. Y.; Humphreys, C. J.; Sutton, A. P. Electron-Energy-Loss Spectra and the Structural Stability of Nickel Oxide: An LSDA+*U* study. *Phys. Rev. B: Condens. Matter Mater. Phys.* **1998**, *57*, 1505−1509.
(58) Nørskov, J. K.; Rossmeisl, J.; Logadottir, A.; Lindqvist, L.; Kitchin, J. R.; Bligaard, T.; Jonsson, H. Origin of the Overpotential for Oxygen Reduction at a Fuel-Cell Cathode. *J. Phys. Chem. B* **2004**, *108* (46), 17886−17892.

https://doi.org/10.1021/acsnano.0c09905
ACS Nano 2021, 15, 11218−11230